Comprehensive monitoring of tissue composition using in vivo imaging of cell nuclei and deep learning

Amrita Das Gupta[a], Livia Asan[a,d], Jennifer John [a], Carlo A. Beretta [a], Thomas Kuner [a], Johannes Knabbe [a,b]

a Department of Functional Neuroanatomy, Institute for Anatomy and Cell Biology, Heidelberg University, Germany.

b Department of General Psychiatry, Centre for Psychosocial Medicine, Heidelberg University, Germany.

d Current address: Department of Neurology and Center for Translational Neuro- and Behavioral Sciences (C-TNBS), University Hospital Essen, Germany.

Correspondence: johannes.knabbe@uni-heidelberg.de, thomas.kuner@uni-heidelberg.de

Abstract

Comprehensive analysis of tissue composition has so far been limited to ex vivo approaches. Here, we introduce NuClear (Nucleus-instructed tissue composition using deep learning), an approach combining in vivo two-photon imaging of histone 2B-eGFP-labeled cell nuclei with subsequent deep learning-based identification of cell types from structural features of the respective cell nuclei. This allowed us to classify all cells per imaging volume (0.25 mm^3 containing ~25000 cells) and identify their position in 3D space in a non-invasive manner using only a single label. NuClear opens a window to study changes in relative abundance and location of all major brain cell types in individual mice over extended time periods, enabling comprehensive studies of changes in cellular composition in physiological and pathophysiological conditions.

121 words

Introduction

Understanding the plasticity and interaction of different brain cell types in vivo has been a limiting factor for the investigation of large-scale structural brain alterations associated with diverse physiological and pathophysiological states. Until now, to investigate the effect of an experimental intervention on all brain cell types and their respective spatial interaction, each cell type would require an individual labelling strategy using a set of specific promoters and fluorophores. This would require prioritizing cell types from the outset and thereby limit the scope to a small subset of the population. With multiple cell types to consider, the number of experiments and animals investigated may become intractable. So far, studies quantitatively assessing whole tissue composition have analyzed tissue ex vivo using manual or automated analysis of antibody staining

in tissue slices (Ero, Gewaltig et al. 2018) or after isotropic fractionation (Herculano-Houzel and Lent 2005), in situ hybridization (Nagendran, Riordan et al. 2018) or single cell sequencing (Zeisel, Hochgerner et al. 2018). Other studies were using manual (Schmitz and Hof 2007) or automated stereological approaches (Zhang, Yan et al. 2017, Pakkenberg, Olesen et al. 2019). All these studies were conducted ex vivo and, in part, require the dissolution of the studied organ's cellular architecture. The ability to identify all brain cell types and their location in 3D space, here referred to as 'composition', in the integrity of the living brain to quantify and observe changes over time is enticing. Here, we propose an experimental approach to study neurons and glial cells, especially, astroglia, microglia and oligodendroglia, as well as endothelial cells in the same mouse in vivo, using only one genetically modified mouse line expressing a fusion protein of Histon 2B and enhanced green fluorescent protein (eGFP) in all cell nuclei. Our approach uses a deep learning method, implementing artificial neural networks to classify each nucleus belonging to a specific cell type, making it possible to perform a nucleus-instructed tissue composition analysis using deep learning (NuClear). In addition, knowing the 3D location of every cell opens new opportunities for further analyses. Apart from the application in longitudinal in vivo imaging of the mouse brain, the concept of this technique will be applicable to many other cellular imaging techniques and in different experimental systems, making it a powerful approach for future analyses of large-scale automated tissue composition.

384 words

59 **Results**

60 For the comprehensive identification and tracking of cell type-composition in the mouse brain
61 over the course of weeks and even months, a mouse line constitutively expressing a human
62 Histone 2B-eGFP (H2GFP) fusion protein in all cell nuclei was imaged using 2-photon microscopy
63 after implantation of a chronic cranial window (Figure 1A, Supplementary Figure 1A, B).
64 Volumetric images taken from this mouse line resemble the well-known DAPI staining of cell
65 nuclei (Supplementary Figure 1C). For automated cell type classification of the imaged nuclei, a
66 neuronal network was trained on images of GFP-labeled nuclei from reporter mouse lines, where
67 known cell types were additionally labelled with a red fluorescent protein (tdTomato or mCherry),
68 thus creating a ground truth dataset for supervised training for each cell type (Figure 1B, lower
69 panel). The trained neuronal network was used to classify cell types based on their GFP-labeled
70 nuclei (Figure 1B, upper panel). In our study we selected five different cell types for classification
71 (Figure 2A): Neurons (yellow), astroglia (blue), microglia (green), oligodendroglia (turquoise), and
72 endothelial cells (red). To generate ground-truth datasets without a bleed through of the strong
73 tdTomato fluorescence towards the GFP-channel (Supplementary Figure 1D), we chose a method
74 of inducing the expression of tdTomato for unequivocal cell type identification *after* imaging of
75 the nuclei. We selected a labelling strategy consisting of a tamoxifen-inducible cell type-specific
76 Cre-recombinase in conjunction with a floxed-tdTomato mouse line for endothelial cells (Tie2-
77 CreErt2), astroglia (GFAP-CreErt2) and oligodendroglia (PLP-CreErt2) (Figure 2B). We acquired
78 volumetric images of nuclei from these mouse lines and induced tdTomato expression via
79 intraperitoneal injection of tamoxifen (Supplementary Figure 1E). After 3 to 4 days the same
80 location was imaged again, and the previously imaged nuclei were selected by overlay with the

red fluorescence signal (Figure 2C). As microglia changed their positions after induction with tamoxifen, we chose acute injection of tomato-lectin coupled to DyLight 594 to label these cells, which did not produce any signal alterations in the eGFP-channel (Supplementary Figure 1F). Neurons were labelled using an AAV-mediated expression of the mCherry red fluorescent protein under the neuron-specific synapsin promotor (syn1-mCherry), which did not affect the eGFP-signal due to its specific fluorescence properties (Supplementary Figure 1F). Hence, this approach was used to ascertain images of the labeled nuclei to be undisturbed by signals possibly arising from the red fluorescence used for unequivocal identification of the cell type.

Automated segmentation of nuclei in the raw data was achieved using the Stardist neuronal network (Schmidt, Weigert et al. 2018), trained on manually labeled ground truth datasets of the H2GFP mouse line which achieved a high detection accuracy of 94 % as well as a good shape segmentation (Supplementary Figure 1G, H). From the binary mask of individual nuclei and their respective pixel intensities in the raw image, in total 121 features were extracted, including 3D-diameter, flatness, grey level non-uniformity, entropy, first order minimum or coarseness (Figure 2D) (for a full list see Supplementary Table 1). To reduce overfitting of the classification algorithm, a subset of 12 features representing the whole feature space was chosen by a feature selection algorithm (Supplementary Table 2). A polar plot with these nuclear features visualizes the differences between the cell types, for example neuronal nuclei having a larger 3D diameter and minor axis length in comparison to microglial and astroglial nuclei that exhibit a larger pixel entropy (Figure 2E). For certain features, significant differences between the cell types can be shown as well, for example flatness being significantly higher in nuclei of microglia than in nuclei of neurons (Figure 2F). Furthermore, combinations of two or three distinctive features allow for

103 the visual separation of the cell types in the 2D and 3D space, respectively (Supplementary Figure
104 2). Having demonstrated the ability of nuclear features to distinguish between their
105 corresponding cell types, we created a neuronal network for cell type classification based on
106 nucleus features (Supplementary Figure 3). Using data from the five reporter mouse lines, we
107 trained one classifier per cell type for distinguishing one cell type from the respective other cell
108 types (Figure 3A). To increase the amount of training data and equalize the nucleus counts for
109 each cell type to reduce training bias, synthetic data was generated from the features of the
110 original dataset. Synthetic data distribution fit well to the distribution of the original data for each
111 cell type (Supplementary Figure 4A, B). Training and validation were performed on a dataset
112 consisting of original and synthetic data (Figure 3A). After classifying the whole dataset, nuclei
113 were either assigned to a single class, two or more classes (undecided) or to none (unclassified).
114 Precision and recall rates for each classifier were high for neurons and endothelial cells. Due to
115 their relative similarity, glial cells exhibited lower precision and recall rates (Figure 3B). After
116 combining all classifier output, the classification accuracy for the entire dataset was highest for
117 neurons (98 %) and endothelial cells (99 %), whereas the classifier showed lower accuracies for
118 all glial cell types, especially for microglia (96 %) (Figure 3C, D, for the respective confusion plots
119 see Supplementary Figure 5). A model classifying only neurons, glia (as one common class
120 irrespective of glial subtype) and endothelial cells showed even higher accuracy, precision and
121 recall rates for glial cells (data not shown). When applying the classification model to data of
122 cortical layer 2/3 of the supplementary motor area (SMA) of H2GFP mice, two features not chosen
123 for classification by the automated feature selection algorithm differed significantly between the
124 classes: neuronal nucleus volume (Figure 3E) and endothelial mean surface to volume ratio, a

125 measure for the sphericity of the nucleus (Figure 3F). Both findings are expected for each of the
126 cell types and hence demonstrate that also features that were not used for classification can be
127 readily detected. The 3D classification results for one example volume containing 20123 cells are
128 shown in Supplementary Figure 6 and intuitively visualize the relative abundance and positioning
129 of cell types within the volume and their mutual spatial relationship (see also Supplementary
130 Movie 1 for an animated version of the segmentation and classification process). The absolute
131 nuclei count from the region shows a density of 44000 neurons/mm³ and of 57000 glial cells
132 (including unclassified cells), resulting in a Glia/Neuron-Ratio of 1.3 (Figure 3G). The number of
133 cells in a subset of Layer2/3 over 12 weeks remained unchanged after correcting for multiple
134 comparisons (Figure 3H). When normalizing these counts to baseline, only the number of
135 astrocytes shows a trend to increase (Figure 3I), which could be either due to astrocytosis caused
136 by aging or caused by continued reaction to the chronic window implantation. Interestingly,
137 astrocytic nuclear volume significantly decreases over time (Figure 3J), which might be due to
138 altered transcriptional activity known to occur in astrocytes with aging (Boisvert, Erikson et al.
139 2018, Clarke, Liddelow et al. 2018). This latter result illustrates that our method can extract even
140 subtle and unexpected changes from of a vast parameter space of different aspects of tissue
141 composition.
142 1157 words
143
144 **Discussion**
145 Here, we present a novel method for intravital, longitudinal, comprehensive, large scale and 3D
146 tissue composition based on a deep learning algorithm trained on radiomics features of cell nuclei

147 (NuClear -- Nucleus-instructed tissue composition using deep learning). We demonstrate that cell
148 types can be distinguished via the respective properties of their cell nucleus. This has been mostly
149 anecdotal anatomical textbook knowledge for a good century, yet it has rarely been quantified
150 and compared in a systematic manner. Moreover, we demonstrate how this rejuvenated
151 anatomical knowledge can be converted into a powerful new approach with the help of today's
152 state-of-the-art imaging and deep learning techniques.

153 For a demonstration of the usability of NuClear, we analyzed volumetric images of the cortex of
154 H2GFP mice acquired with in vivo two photon microscopy. To be able to image a large dataset in
155 a comparatively short time, we chose a feasible imaging resolution with a z-step size of 2 µm and
156 a lateral resolution of 0.3 µm. We were able to image a whole 3D volume of 700 μm^3 consisting
157 of more than 20000 cells in around 20 minutes, making it possible to perform large scale data
158 acquisition in a repeated manner, enabling longitudinal intravital monitoring of tissue histology
159 over time and in response to perturbations, treatments, or adaptive processes.

160 Neurons and endothelial cells showed the best classification results regarding total classification
161 accuracy and precision as well as recall rates, as their nucleus feature profile turned out to be
162 markedly different between each other as well as between the individual glial cell types (Figure
163 2E, 3B). Differentiation between the three different glial cell types was more difficult to achieve,
164 resulting in lower overall accuracy rates as well as lower precision and recall rates, due their
165 respective nucleus feature profiles being more similar. Nevertheless, with an accuracy above 90%
166 our approach can reliably be used to subclassify glia. We expect that a higher imaging resolution
167 as well as more training data would increase the classifier performance even more. Another
168 reason for the comparatively lower classification accuracy in microglia might be that we used

169 acute injection of tomato-lectin to label these cells, which could have introduced a bias towards
170 activated microglia. Nevertheless, the overall accuracy of the microglia classifier for the whole
171 training dataset was around 96%, owing to the fact, that non-microglial nuclei could be identified
172 correctly most of the time. For astrocytes, we used GFAP-labelled cells for classification, a label
173 that primarily marks reactive astrocytes and is expressed increasingly during aging. Future studies
174 could optimize this labelling strategy. Further support for the accuracy of the classifier can be
175 concluded from analyzing features of nuclei that were not used during training such as mean
176 nuclear volume and surface to volume ratio. These features showed distinct clustering and low
177 standard deviation in each class as well as significant differences between the cell types.
178
179 When applying the classification model to a Layer 2/3 volume of the supplementary motor area
180 (SMA) and extrapolating the number of cells per mm^3, a marked similarity of the number of
181 neurons with published results is evident (43822 ± 3747 vs 45374±4894) (Ero, Gewaltig et al.
182 2018) (Figure 3G). Astrocyte numbers are similar (18882 ± 3848 vs 13258± 1416), microglia
183 numbers differ more (12573 ± 2840 vs 24584.6± 2687). Oligodendrocyte numbers seem to be
184 vastly different (4358 ± 586 vs 51436.1± 488), which might stem from the fact that only Layer 2/3
185 was analyzed, excluding deeper cortical layers that have been shown to contain the majority of
186 oligodendrocytes (Tan, Kalloniatis et al. 2009). When all glial cells as well as undecided and
187 unclassified cells are summed up, a Glia/Neuron ratio of 1.3 can be calculated, a result that is in
188 line with known results of the rodent cortex (Herculano-Houzel 2014). Candidates for unclassified
189 cells could be the relatively large population of oligodendrocyte precursor cells (about 5% of all
190 cells in the brain (Dawson, Polito et al. 2003)), which might explain that unclassified nuclei have

191 a similar volume as oligodendrocytes (Figure 3E). In conclusion, cell type counts are comparable
192 to published results.
193
194 A decisive advantage of NuClear over existing ex vivo methods is the ability to study cell type
195 changes over time in the same imaging volume and thus achieving a higher statistical power in
196 experiments with fewer animals, which is crucial for complying with the “3R” rules in animal
197 research (reduce, replace, refine). In our lab, we were able to perform imaging in selected
198 locations up to 1 year after the implantation of chronic cranial windows. When analyzing the
199 effect of time on the imaging volumes from the supplementary motor area (SMA), we were able
200 to detect a trend towards astrocytosis after 12 weeks, which might be due to the aging process
201 leading to a higher GFAP-reactivity (Palmer and Ousman 2018). The significant decrease in mean
202 nucleus volume of astroglia over time could be attributed to altered transcriptional activity since
203 astrocyte reactivity changes in the cortex over time (Clarke, Liddelow et al. 2018). Another factor
204 explaining the astrocytosis might be the constant reaction to the chronic cranial window (Guo,
205 Zou et al. 2017).
206
207 Our study illustrates only one possible application of NuClear and subsequent analysis of 3D tissue
208 composition. Here we focused on the identification of cell types, but the 3D datasets generated
209 allow for additional analyses such as statistical distribution of cell types with regard to each other,
210 their nearest neighbor distances or inferences on physical tissue volume (Asan, Falfan-Melgoza et
211 al. 2021). Our classifiers mostly rely on geometrical parameters such as nucleus shape, but also
212 considers texture information to a certain degree. An increased sampling resolution may further

213 increase textural information and thereby yield even higher classification accuracies. NuClear will
214 be easily applicable to different organs, other organisms, and in vitro preparations such as cell
215 cultures or organoids, provided that the respective ground truths are available. It will be usable
216 with a variety of microscopy techniques such as confocal-, light-sheet- or three-photon
217 microscopy, making large-scale tissue analysis much more accessible. We anticipate that any cell
218 type will be detected by adding more classifiers trained with appropriate ground truth data. In
219 this way, we propose an easy and readily usable method to implement large-scale tissue analysis
220 ex vivo or in vivo to study effects of interventions on cell type compositions of different organs.
221 1050 words
222
223
224 **Materials and Methods**
225
226 Ethical approval
227 The entire study was conducted in line with the European Communities Council Directive
228 (86/609/ECC) to reduce animal pain and/or discomfort. All experiments followed the German
229 animal welfare guidelines specified in the TierSchG. The study has been approved by the local
230 animal care and use council (Regierungspräsidium Karlsruhe, Baden-Wuerttemberg) under the
231 reference numbers G294/15 and G27/20. All experiments followed the 3R principle and complied
232 with the ARRIVE guidelines (Percie du Sert, Hurst et al. 2020).
233
234 Animals

235 Adult transgenic mice expressing the human histone 2B protein (HIST1H2B) fused with enhanced
236 green fluorescence protein (eGFP) under the control of the chicken beta actin promoter (CAG-
237 H2B-eGFP) (Hadjantonakis and Papaioannou 2004) (B6.Cg-Tg(HIST1H2BB/EGFP)1Pa/J, Jackson
238 Laboratory; # 006069) were used in all animal experiments. For the reporter mouse lines, H2B-
239 eGFP mice were bred to carry a floxed sequence of the red fluorescent protein tdTomato and a
240 tamoxifen inducible Cre-recombinase under the expression of different cell type specific
241 promoters: GFAP for astroglia (HIST1H2BB/EGFP-GFAP/ERT2CRE-
242 CAG/loxP/STOP/loxP/tdTomato), PLP for oligodendroglia (HIST1H2BB/EGFP-PLP/ERT2CRE-
243 CAG/loxP/STOP/loxP/tdTomato) and Tie2 for endothelial cells (HIST1H2BB/EGFP-Tie2/ERT2CRE-
244 CAG/loxP/STOP/loxP/tdTomato). Expression of the Cre-recombinase was achieved over a course
245 of up to 5 days with daily intraperitoneal injection of two doses of 1mg Tamoxifen (Sigma Life
246 sciences; dissolved in 1 part ethanol (99.8% absolute) and 10 parts sunflower oil) (supp. Figure 1
247 D). Microglia were visualized using intracortical injection of Lycopersicon Esculentum (Tomato)
248 lectin coupled with DyLight 594 during the cranial window surgery after dilution by 1:39 in
249 150mM NaCl, 2.5 mM KCl, 10mM HEPES at pH 7.4 (Schwendele, Brawek et al. 2012)
250 (supplementary Figure 1E). For neuronal labelling, an in house produced adeno-associated virus
251 expressing mCherry under the Synapsin promotor was cortically injected during the cranial
252 window surgery.
253
254 <u>Chronic cranial window implantation</u>
255 A craniectomy procedure was performed on each mouse to enable in vivo two-photon imaging
256 following a predefined protocol as described before (Holtmaat, Bonhoeffer et al. 2009)

257 (Supplementary Figure 1A). Briefly, the mice were anesthetized with an intraperitoneal injection
258 (i.p.) of a combination of 60 µl Medetomidine (1mg/ml), 160 µl Midazolam (5 mg/ml) and 40 µl
259 Fentanyl (0.05 mg/ml) at a dosage of 3 µl/g body weight. The head was shaved, and the mice
260 were fixed with ear bars in the stereotactic apparatus and eye ointment was applied. Xylocain®
261 1 % (100 µl, Lidocaine hydrochloride) was applied under the cranial skin and 250 µl Carprofen (0.5
262 mg/ml) was injected subcutaneously (s.c.). The skin was removed to expose the skull and the
263 surface of the skull was made rough to allow the cement to adhere better. A skull island (approx.
264 6mm ∅) was drilled centered at 1 mm rostral to bregma using a dental drill and removed with a
265 forceps (#2 FST by Dumont) making sure not to damage the cortical surface. For improved imaging
266 condition, the dura was carefully removed from both hemispheres using a fine forceps (#5 FST by
267 Dumont). Normal rat ringer solution (NRR) was applied on the exposed brain surface to keep it
268 moist, and a curved cover glass was placed on top to cover it (Asan, Falfan-Melgoza et al. 2021).
269 With dental acrylic cement (powder: Paladur, Kulzer; activator: Cyano FAST, Hager & Werken
270 GmbH) the cover glass was sealed, and excess cement was used to cover the exposed skull and
271 edges of the skin. A custom designed 3-D printed holder was placed on top of the window and
272 any gaps were filled with cement to ensure maximum adhesion with the skull. After the
273 procedure, the mice were injected (i.p. / s.c.) with a mix of 30 µl Atipamezole (5 mg/ml), 30 µl
274 Flumazenil (0.1 mg/m) and 180 µl Naloxon (0.4 mg/ml) at a dosage of 6 µl per gram body weight.
275 To ensure proper recovery of the mice, 3 more doses of Carprofen were given every 8-12 hours
276 and the mice were placed onto a heating plate and monitored.
277
278 <u>In vivo two photon imaging</u>

279 Two photon imaging was carried out with a two-photon microscope (TriM Scope II, LaVision
280 BioTec GmbH) with a pulsed Titanium-Sapphire (Ti:Sa) laser (Chameleon Ultra 2; Coherent) at
281 excitation wavelengths of 860nm for DyLight 594 and 960nm for H2GFP, tdTomato and mCherry
282 respectively. A water immersion objective (16x; NA 0.8, Nikon) was used to obtain volumetric 3D
283 stacks. Individual frames consisted of 694 µm x 694 µm in XY with a resolution of 0.29 µm/pixel.
284 Stacks were obtained at varying depths up to 702 µm from the cortical surface with a step size of
285 2 µm in Z. Prior to each imaging session, the laser power was adjusted to achieve the best signal
286 to noise ratio. Adaptations were made to minimize the effect of laser attenuation due to tissue
287 depth by creating a z-profile and setting the laser power for different imaging depths while
288 making sure to minimize oversaturation of pixels.
289 Mice were initially anesthetized using a vaporizer with 6% isoflurane, eye ointment was applied.
290 Mice were fixed in a custom-built holder on the microscope stage. Isoflurane was reduced to 0.5
291 – 1.5% depending on the breathing rate of each mouse to achieve a stable breathing rate of 55 –
292 65 breaths per minute with an oxygen flow rate of 0.9 – 1.1 l/min. A heating pad was placed
293 underneath the mouse to regulate body temperature. An infrared camera was used for
294 monitoring of the mice during the imaging.
295 Reporter mouse lines for neurons, astroglia, oligodendroglia and endothelial cells were imaged
296 3-4 weeks after the cranial window surgery. Microglia reporter mice were imaged immediately
297 after the cranial window surgery for a minimal inflammatory reaction (for a full list of reporter
298 mice see supplementary Figure 4E). For imaging adult H2GFP mice, 3D volumetric stacks were
299 imaged in the supplementary motor area (SMA) at two different timepoints. This includes
300 baseline imaging which was performed at 3-4 weeks after the chronic cranial window surgery and

301 in week 12 after the baseline. To investigate a possible age effect, mice underwent a sham surgery
302 at the left hindpaw 1 week after baseline surgery as part of a different study.
303
304 Automatic nuclei segmentation using StarDist
305 Automated nuclei segmentation was achieved using the StarDist algorithm, which implements a
306 machine learning method using a neuronal network to detect star-convex polygons in 2D and 3D
307 fluorescence imaging (Schmidt, Weigert et al. 2018). The StarDist model was trained to segment
308 nuclei in 3D using an in-house developed Jupyter Notebook. Manually segmented and labelled
309 nuclei from 15 different crops from the two-photon volumetric data with approximately 150 –
310 200 nuclei each were used for training the StarDist 3D segmentation classifier (supplementary
311 Figure 1 H).
312 Detection accuracy and precision were calculated by counting the true positive nuclei (TP), false
313 positive nuclei (FP) and false negative nuclei (FN). 4 arbitrary volumetric images were selected
314 containing up to 80 nuclei per crop. Accuracy was calculated as TP / (TP + FP + FN). Precision was
315 calculated as TP / (TP + FP).
316
317 Feature extraction using PyRadiomics
318 Using the PyRadiomics python package (van Griethuysen, Fedorov et al. 2017), in total 107
319 radiomics features were extracted for each segmented nucleus including, but not limited, to
320 morphological features, intensity features and texture features (see supplementary Table 1).
321 Nuclei touching the borders of the imaging volume were excluded.
322

323 Extraction of data for training of the classifier

324 For supervised training of the deep neural network for cell type classification, a ground truth
325 dataset was created using the two-photon volumetric fluorescence data and automatically
326 segmented nuclei. Using the red fluorescence channel, nuclei belonging to a specific cell type
327 were manually identified by overlaying the green channel data. This allowed for manual
328 identification of the label ID from the StarDist output by synchronizing the two imaging volumes
329 in ImageJ/Fiji and extraction of features from PyRadiomics for these individual nuclei.
330 Approximately 70-150 nuclei were identified for each cell type (supp. Figure 5).
331 To increase the number of nuclei for training and make it equal in size for all cell types to avoid a
332 bias in training, synthetic datasets were created from nuclei features using the synthetic data
333 vault (SDV) package (Patki, Wedge et al. 2016), which utilizes correlations between features of
334 the original dataset as well as mean, minimum or maximum values and standard deviations. The
335 synthetic data generated by the model fit to the original dataset with approximately 83% accuracy
336 (supplementary Figure 5).
337

338 Training of the classification model

339 All training and validation of the classifiers were performed with a custom MATLAB (R2021a,
340 Mathworks) script, manual validation was performed in ImageJ/Fiji. Original and synthesized data
341 were merged into a single table and random indices were generated to divide the dataset into a
342 training, test, and validation dataset with 70%, 15% and 15% of the total dataset, respectively.
343 The same training, test, and validation datasets were used for training five different classifiers,
344 one for each cell type. In the training dataset, for each classifier, the class of interest was assigned

345 a unique identifier and all other cell classes were denoted by another identifier, for example,
346 when training the neuronal classifier, the neurons were labelled as “Neuron” while all the other
347 cell types in the dataset were labelled “Other” (supplementary Figure 3). Each classification
348 network had the same design. Initially, a sequential feature selection algorithm “sequentialfs”
349 was applied to the whole dataset to extract 12 features with the highest variability to reduce data
350 overfitting. These were fed into the “feature input layer” of the classifier. The features were z-
351 score normalized for better compatibility between each class. A “fullyconnected” layer of 50
352 outputs was created and a mini-batch size of 16 samples was set to reduce the time and memory
353 consumption during training. A batch normalization layer was added to reduce sensitivity to the
354 initialization of the network. The activation layer ReLU (Rectified Linear Unit) was added for
355 thresholding operations. Another “fullyconnected” layer was added, which sets the number of
356 outputs identical to the number of input classes and a second activation layer “softmax” was
357 chosen for classifying the output into the two separate groups. The “adam” adaptive moment
358 estimation optimizer was selected as the solver for the training network which updates the
359 network weights based on the training data in an iterative manner. The training data and the
360 validation data were shuffled every epoch before training and network validation, respectively.
361 After each classifier was trained, further automatic and visual validation was performed to check
362 for accuracy.
363

364 <u>Classification of the H2GFP data</u>

365 After imaging of the volumetric volume of H2GFP nuclei, automated segmentation of all nuclei
366 was performed with the StarDist neuronal network (see above, supplementary Figure 6).

367 Afterwards, features for every segmented nucleus were extracted using PyRadiomics (see
368 above). Every segmented nucleus was then classified with all the five different classifiers. Thus, a
369 single nucleus would be either labelled as belonging to one of the five classes or to the "Other"
370 class. Nuclei that were assigned to multiple classes, were labelled as "Undecided" (UD). Any
371 nuclei that were identified as "Other" by all the classifiers were labelled as "Unclassified" (UC).
372

373 Statistical analysis

374 All classified nuclei and their features were stored in a local MySQL database (MySQL Workbench
375 8.0). The data were imported into R (R. Core Team 2021) for statistical analysis. Cell count, mean
376 nuclei volume and first nearest neighbor distance were calculated for each cell type for different
377 timepoints. The nearest neighbor distance was calculated using the "spatstat" package for R
378 (Baddeley and Turner 2005). Depending on the distribution of the data either t-tests or non-
379 parametric statistical test (Wilcoxon signed-rank test) were used for statistical testing, p-values
380 were corrected for multiple comparisons using the "Bonferroni"-method. Plots were created
381 using the R package "ggplot2" (Wickham 2016).
382

383 **Contributions**

384 ADG: Data acquisition, implementation and development of segmentation and classification
385 pipeline, training of classifiers, conceptual inputs, generation of figures, writing of the MS.
386 LA: Acquisition of experimental ground truth data with reporter mouse lines using 2PLSM imaging
387 and establishment of tomato-lectin labelling, proof-of-concept with initial development of
388 solutions for segmentation and classification.

CAB: Development of segmentation, application of StarDist, contributions to classification.

JJ: Data acquisition, training of StarDist for segmentation.

TK: Initial project idea and concept, writing of the MS, supervision.

JK: Conceptualization, implementation, experimentation, analysis, writing of the MS, project management and supervision.

Acknowledgements

We want to thank Michaela Kaiser for her excellent technical support during preparation and execution of experiments. We gratefully acknowledge the support by the German Research Foundation (DFG) (SFB1158, project B08 awarded to TK), the data storage service SDS@hd, supported by the Ministry of Science, Research and the Arts Baden-Württemberg (MWK) and the DFG through grant INST 35/1314-1 FUGG, as well as the high-performance cluster bwForCluster MLS&WISO, supported by the MWK and the DFG through Grant INST 35/1134-1 FUGG.

411 **References**

412 Arganda-Carreras, I., C. O. S. Sorzano, J. Kybic and C. Ortiz-de-Solórzano (2008). bUnwarpJ :
413 Consistent and Elastic Registration in ImageJ . Methods and Applications.
414 Asan, L., C. Falfan-Melgoza, C. A. Beretta, M. Sack, L. Zheng, W. Weber-Fahr, T. Kuner and J.
415 Knabbe (2021). "Cellular correlates of gray matter volume changes in magnetic resonance
416 morphometry identified by two-photon microscopy." Sci Rep 11(1): 4234.
417 Baddeley, A. and R. Turner (2005). "spatstat: An R Package for Analyzing Spatial Point Patterns."
418 Journal of Statistical Software 12(6): 1 - 42.
419 Boisvert, M. M., G. A. Erikson, M. N. Shokhirev and N. J. Allen (2018). "The Aging Astrocyte
420 Transcriptome from Multiple Regions of the Mouse Brain." Cell Rep 22(1): 269-285.
421 Clarke, L. E., S. A. Liddelow, C. Chakraborty, A. E. Munch, M. Heiman and B. A. Barres (2018).
422 "Normal aging induces A1-like astrocyte reactivity." Proc Natl Acad Sci U S A 115(8): E1896-
423 E1905.
424 Dawson, M. R., A. Polito, J. M. Levine and R. Reynolds (2003). "NG2-expressing glial progenitor
425 cells: an abundant and widespread population of cycling cells in the adult rat CNS." Mol Cell
426 Neurosci 24(2): 476-488.
427 Ero, C., M. O. Gewaltig, D. Keller and H. Markram (2018). "A Cell Atlas for the Mouse Brain."
428 Front Neuroinform 12: 84.
429 Guo, D., J. Zou, N. Rensing and M. Wong (2017). "In Vivo Two-Photon Imaging of Astrocytes in
430 GFAP-GFP Transgenic Mice." PLoS One 12(1): e0170005.
431 Hadjantonakis, A. K. and V. E. Papaioannou (2004). "Dynamic in vivo imaging and cell tracking
432 using a histone fluorescent protein fusion in mice." BMC Biotechnol 4: 33.

433 Herculano-Houzel, S. (2014). "The glia/neuron ratio: how it varies uniformly across brain
434 structures and species and what that means for brain physiology and evolution." Glia 62(9):
435 1377-1391.
436 Herculano-Houzel, S. and R. Lent (2005). "Isotropic fractionator: a simple, rapid method for the
437 quantification of total cell and neuron numbers in the brain." J Neurosci 25(10): 2518-2521.
438 Holtmaat, A., T. Bonhoeffer, D. K. Chow, J. Chuckowree, V. De Paola, S. B. Hofer, M. Hubener, T.
439 Keck, G. Knott, W. C. Lee, R. Mostany, T. D. Mrsic-Flogel, E. Nedivi, C. Portera-Cailliau, K.
440 Svoboda, J. T. Trachtenberg and L. Wilbrecht (2009). "Long-term, high-resolution imaging in the
441 mouse neocortex through a chronic cranial window." Nat Protoc 4(8): 1128-1144.
442 Nagendran, M., D. P. Riordan, P. B. Harbury and T. J. Desai (2018). "Automated cell-type
443 classification in intact tissues by single-cell molecular profiling." Elife 7.
444 Pakkenberg, B., M. V. Olesen, S. S. Kaalund and K. A. Dorph-Petersen (2019). "Editorial:
445 Neurostereology." Front Neuroanat 13: 42.
446 Palmer, A. L. and S. S. Ousman (2018). "Astrocytes and Aging." Front Aging Neurosci 10: 337.
447 Patki, N., R. Wedge and K. Veeramachaneni (2016). The Synthetic Data Vault. 2016 IEEE
448 International Conference on Data Science and Advanced Analytics (DSAA).
449 Percie du Sert, N., V. Hurst, A. Ahluwalia, S. Alam, M. T. Avey, M. Baker, W. J. Browne, A. Clark,
450 I. C. Cuthill, U. Dirnagl, M. Emerson, P. Garner, S. T. Holgate, D. W. Howells, N. A. Karp, S. E.
451 Lazic, K. Lidster, C. J. MacCallum, M. Macleod, E. J. Pearl, O. H. Petersen, F. Rawle, P. Reynolds,
452 K. Rooney, E. S. Sena, S. D. Silberberg, T. Steckler and H. Wurbel (2020). "The ARRIVE guidelines
453 2.0: Updated guidelines for reporting animal research." PLoS Biol 18(7): e3000410.
454 R. Core Team (2021). "R: A Language and Environment for Statistical Computing."

455 Schmidt, U., M. Weigert, C. Broaddus and G. Myers (2018). Cell Detection with Star-Convex
456 Polygons, Cham, Springer International Publishing.
457 Schmitz, C. and P. R. Hof (2007). Design-Based Stereology in Brain Aging Research. Brain Aging:
458 Models, Methods, and Mechanisms. D. R. Riddle. Boca Raton (FL).
459 Schwendele, B., B. Brawek, M. Hermes and O. Garaschuk (2012). "High-resolution in vivo
460 imaging of microglia using a versatile nongenetically encoded marker." Eur J Immunol 42(8):
461 2193-2196.
462 Tan, S. S., M. Kalloniatis, H. T. Truong, M. D. Binder, H. S. Cate, T. J. Kilpatrick and V. E.
463 Hammond (2009). "Oligodendrocyte positioning in cerebral cortex is independent of projection
464 neuron layering." Glia 57(9): 1024-1030.
465 van Griethuysen, J. J. M., A. Fedorov, C. Parmar, A. Hosny, N. Aucoin, V. Narayan, R. G. H. Beets-
466 Tan, J. C. Fillion-Robin, S. Pieper and H. Aerts (2017). "Computational Radiomics System to
467 Decode the Radiographic Phenotype." Cancer Res 77(21): e104-e107.
468 Wickham, H. (2016). "ggplot2: Elegant Graphics for Data Analysis."
469 Zeisel, A., H. Hochgerner, P. Lonnerberg, A. Johnsson, F. Memic, J. van der Zwan, M. Haring, E.
470 Braun, L. E. Borm, G. La Manno, S. Codeluppi, A. Furlan, K. Lee, N. Skene, K. D. Harris, J. Hjerling-
471 Leffler, E. Arenas, P. Ernfors, U. Marklund and S. Linnarsson (2018). "Molecular Architecture of
472 the Mouse Nervous System." Cell 174(4): 999-1014 e1022.
473 Zhang, C., C. Yan, M. Ren, A. Li, T. Quan, H. Gong and J. Yuan (2017). "A platform for
474 stereological quantitative analysis of the brain-wide distribution of type-specific neurons." Sci
475 Rep 7(1): 14334.
476

Figures

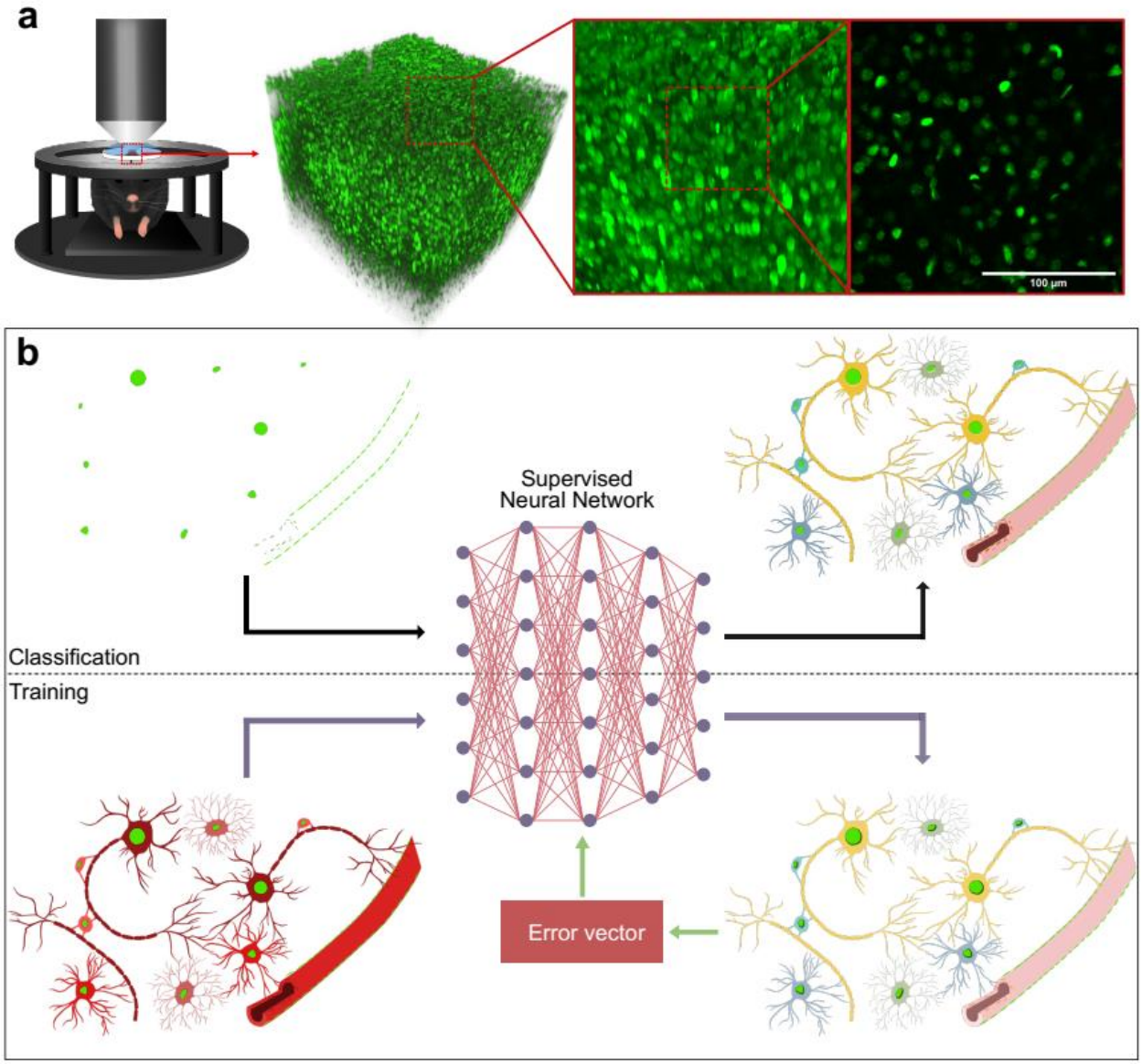

Figure 1. Comprehensive imaging of all cell nuclei and classification into cell types. (a) In-vivo 2-photon microscopy of a 700 µm x 700 µm x 700 µm volume of neocortex. 3D reconstruction and single imaging plane. **(b)** Features of nuclei belonging to identified cell types (red, only one

483 labeled cell type at a time) are used to train a neural network model for the classification of

484 H2GFP-labelled nuclei (green).

485

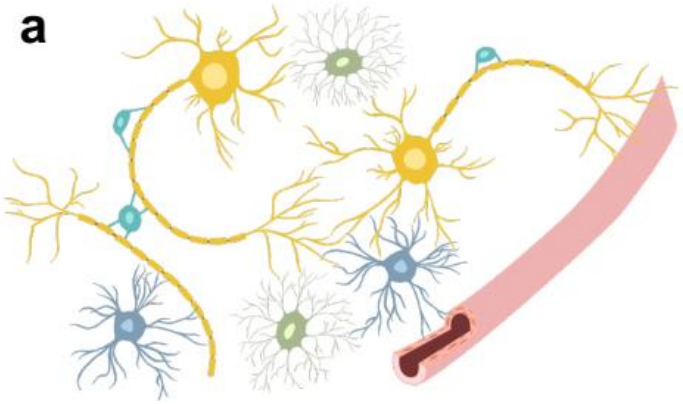

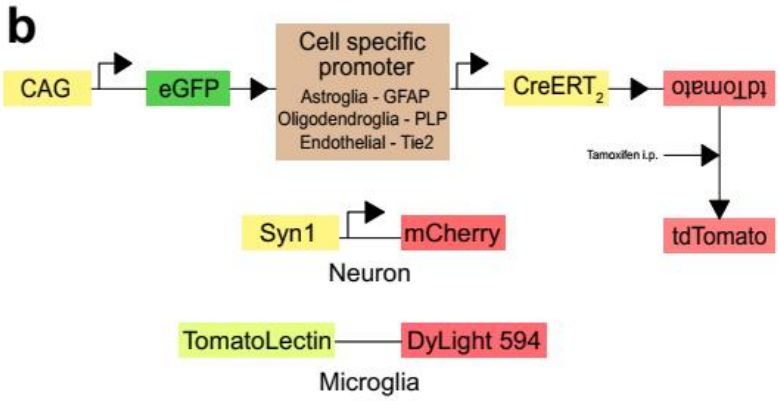
b
CAG
eGFP
Cell specific promoter
Astroglia - GFAP
Oligodendroglia - PLP
Endothelial - Tie2
CreERT2
tdTomato
Tamoxifen i.p.
tdTomato
Syn1
mCherry
Neuron
TomatoLectin
DyLight 594
Microglia

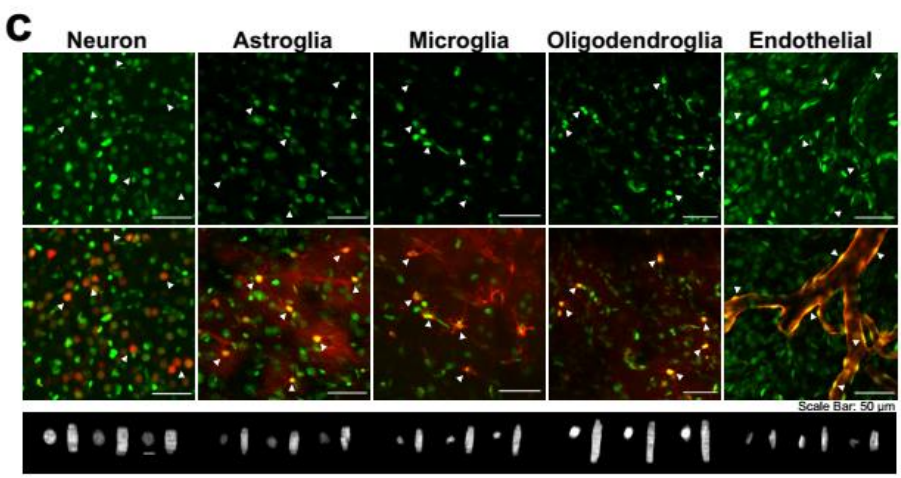
c
Neuron
Astroglia
Microglia
Oligodendroglia
Endothelial
Scale Bar: 50 µm

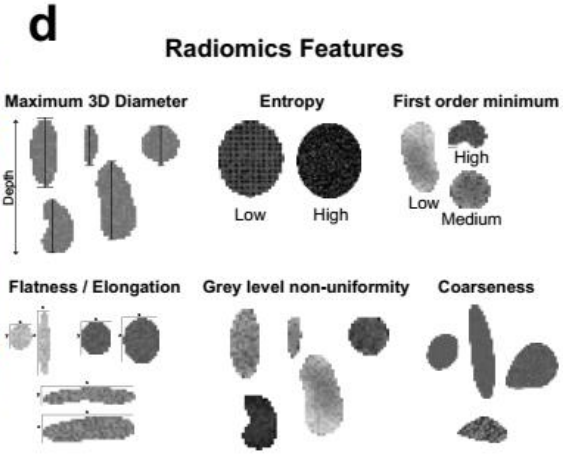
d
Radiomics Features
Maximum 3D Diameter
Depth
Entropy
Low
High
First order minimum
High
Low
Medium
Flatness / Elongation
Grey level non-uniformity
Coarseness

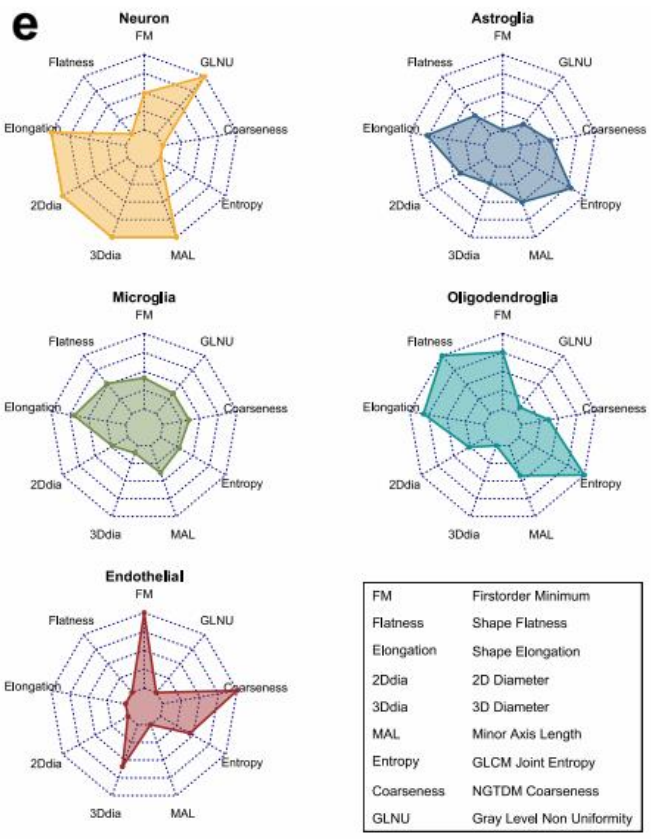
e
Neuron
Astroglia
Microglia
Oligodendroglia
Endothelial
FM
GLNU
Coarseness
Entropy
MAL
3Ddia
2Ddia
Elongation
Flatness
FM Firstorder Minimum
Flatness Shape Flatness
Elongation Shape Elongation
2Ddia 2D Diameter
3Ddia 3D Diameter
MAL Minor Axis Length
Entropy GLCM Joint Entropy
Coarseness NGTDM Coarseness
GLNU Gray Level Non Uniformity

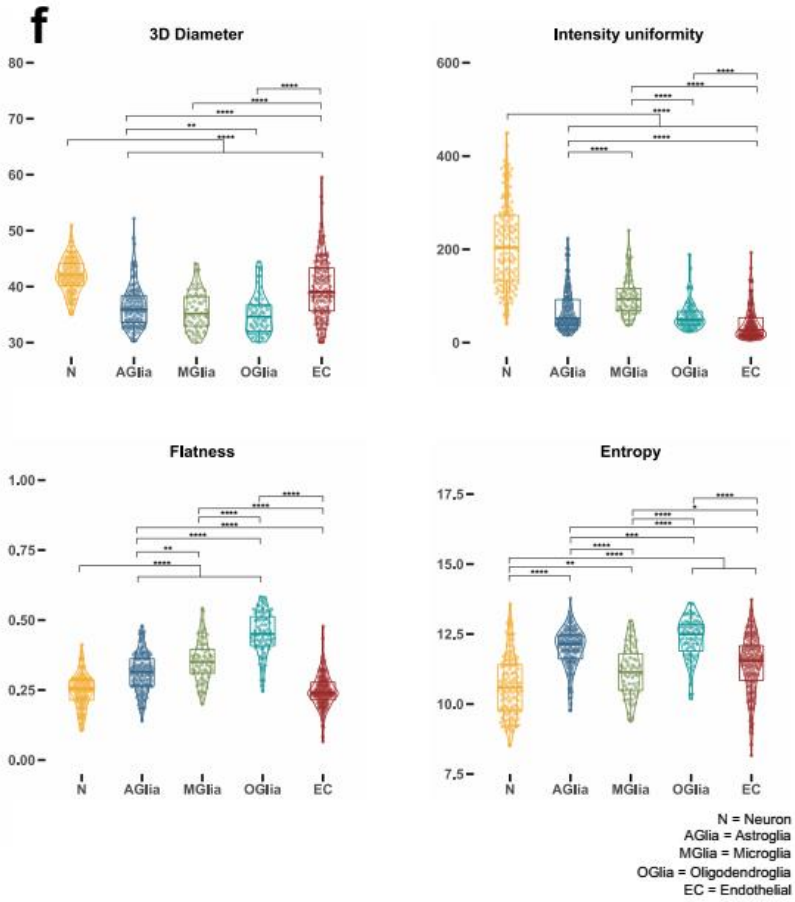
f
3D Diameter
Intensity uniformity
Flatness
Entropy
N
AGlia
MGlia
OGlia
EC
N = Neuron
AGlia = Astroglia
MGlia = Microglia
OGlia = Oligodendroglia
EC = Endothelial

487 **Figure 2. Features of the cell nucleus reveal the corresponding cell type. (a)** Neurons (yellow),
488 astroglia (blue), oligodendroglia (turquoise), microglia (green), endothelial cells (red) were
489 labelled using different strategies **(b). (c)** Nuclei belonging to a specific cell type can be identified
490 by a red fluorescent marker (maximum intensity projections; z = 20 µm). 3D-renderings of
491 individual nuclei are shown in the lower panel. **(d)** Visualization of a subset of radiomics features
492 selected by an algorithm for classification. **(e)** Polar plots showing nuclear features of different
493 cell types. **(f)** Comparison of nuclear features between cell types (Wilcoxon test, n of neurons:
494 135, n of astroglia: 137, n of microglia: 62, n of oligodendroglia: 72, n of endothelial cells: 155, p
495 < 0.05 *, $p < 0.01$ **, $p < 0.001$ ***), N = Neuron, AGlia = Astroglia, MGlia = Microglia, OGlia =
496 Oligodendroglia, EC = endothelial cells.
497

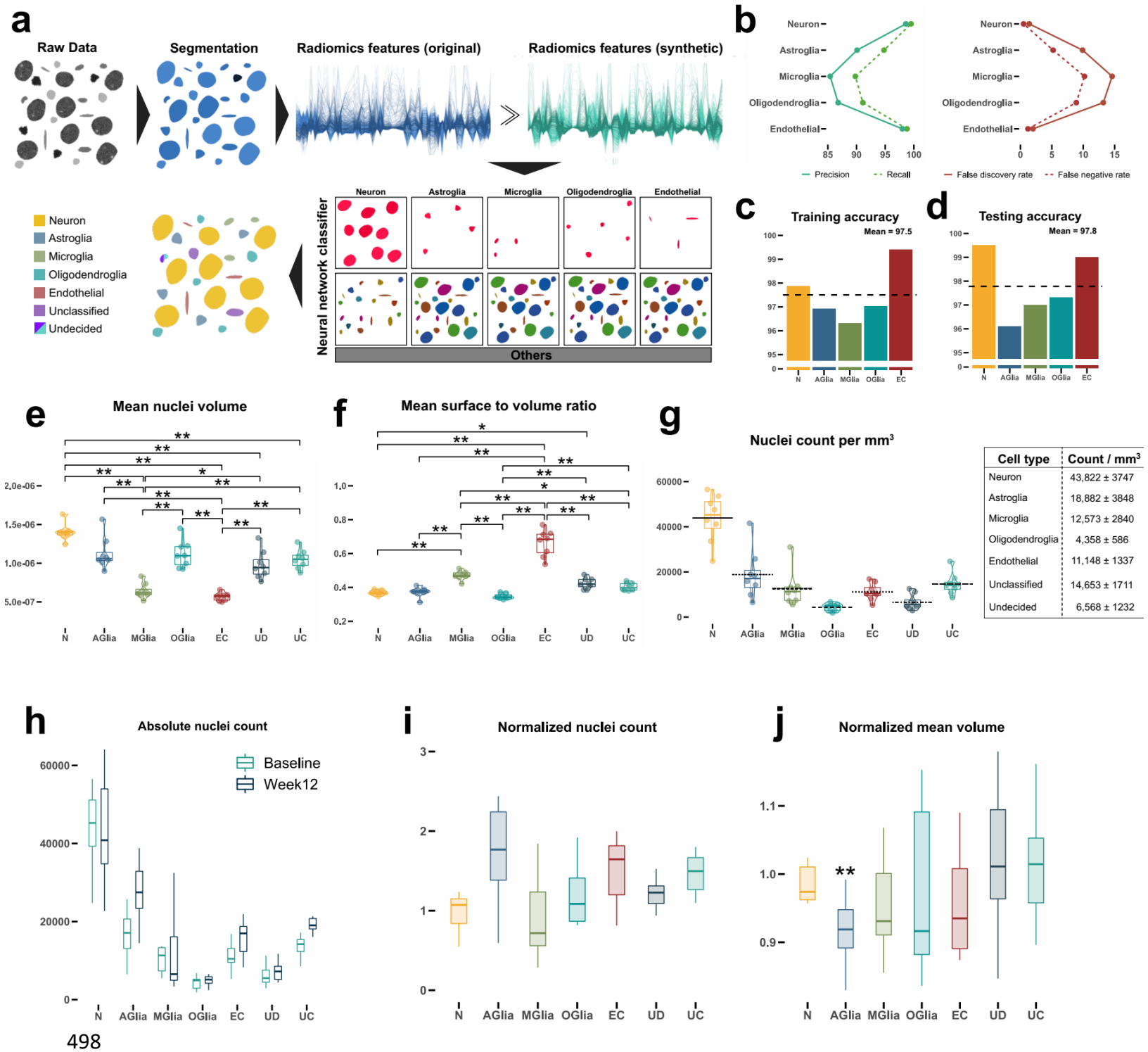

Figure 3. Training a neuronal network for cell type classification. (a) Schematic depiction of the training process. After segmenting raw data with StarDist, features of nuclei were calculated, and

synthetic data was generated. A separate classification network was trained for each cell type. **(b)** Precision, recall, false discovery rate and false negative rates for the test dataset. **(c)** Mean accuracy for all cell types in the training dataset (15 % of the whole dataset). **(d)** Mean accuracy for all cell types in the test dataset (15 % of the whole dataset). **(e)** Comparison of nucleus volume of each cell type. n of neurons: 135, n of astroglia: 137, n of microglia: 62, n of oligodendroglia: 72, n of endothelial cells: 155 **(f)** Comparison of mean surface to volume ratio of each cell type. n of neurons: 135, n of astroglia: 137, n of microglia: 62, n of oligodendroglia: 72, n of endothelial cells: 155 **(g)** Number of nuclei per mm^3., n per class is 8 **(h)** Comparison of the number of nuclei for each cell type between baseline and 12-week timepoint, n per class is 8 **(i)** Comparison of normalized number of nuclei after 12 weeks, n per class is 8 **(j)** Comparison of mean normalized nucleus volume after 12 weeks, n per class is 8 (Wilcoxon test, p-values were corrected for multiple comparisons using the Bonferroni-method, $p < 0.05$*, $p < 0.01$ **, $p < 0.001$ ***), N = Neuron, AGlia = Astroglia, MGlia = Microglia, OGlia = Oligodendroglia, EC = endothelial cells.

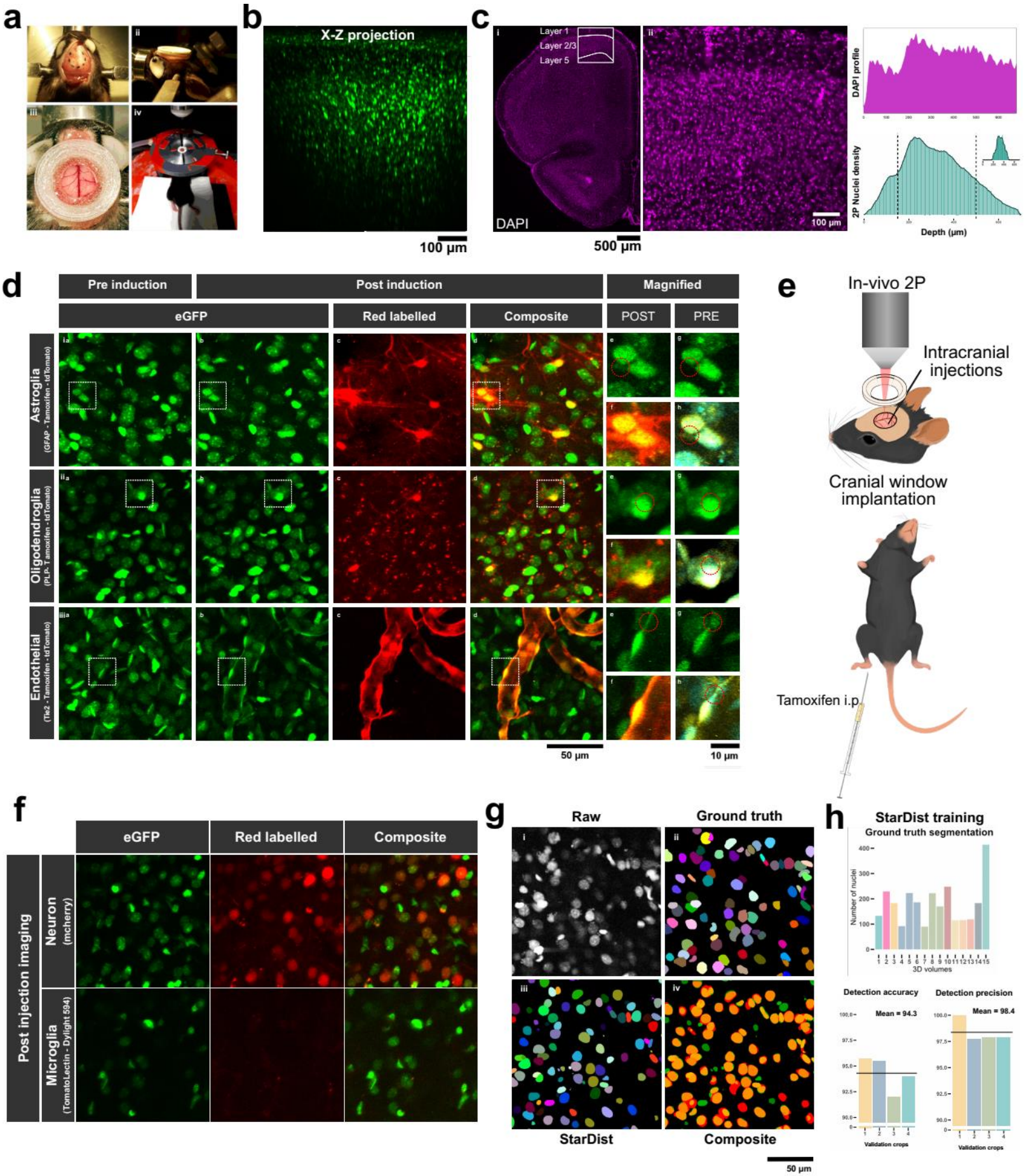
a
b
X-Z projection
100 µm
c
Layer 1
Layer 2/3
Layer 5
DAPI
500 µm
100 µm
DAPI profile
2P Nuclei density
Depth (µm)
d
Pre induction
Post induction
Magnified
eGFP
Red labelled
Composite
POST
PRE
Astroglia
(GFAP - Tamoxifen - tdTomato)
Oligodendroglia
(PLP- Tamoxifen - tdTomato)
Endothelial
(Tie2 - Tamoxifen - tdTomato)
50 µm
10 µm
e
In-vivo 2P
Intracranial injections
Cranial window implantation
Tamoxifen i.p.
f
eGFP
Red labelled
Composite
Post injection imaging
Neuron
(mcherry)
Microglia
(TomatoLectin - Dylight 594)
g
Raw
Ground truth
StarDist
Composite
50 µm
h
StarDist training
Ground truth segmentation
Number of nuclei
3D volumes
Detection accuracy
Mean = 94.3
Detection precision
Mean = 98.4
Validation crops

Supplementary Figure 1 (a) (i,ii,iii) Chronic cranial window implantation using a curved glass cover slip and a custom 3D printed holder. **(iv)** Fixation of the anesthetized mouse in the custom two-photon imaging holder. **(b) (i-iv)** Two-dimensional x-z projection of a two-photon image stack **(c)** Imaging position on a DAPI stained brain slice. Slice thickness 50 µm. DAPI intensity profile showing similar distribution of intensity as a two-photon image of nuclei. The decreasing nucleus density in the two-photon image stack is a result of reduced fluorescence signal at higher depths. Inlay: Nucleus density distribution of sub-volumes used for data analysis. **(d)** Visualization of crosstalk between the eGFP and tdTomato signal after induction with tamoxifen. Overlay of pre (cyan) and post (yellow) GFP after image alignment with the ImageJ plugin bUnwarpJ (Arganda-Carreras, Sorzano et al. 2008).

(e) Intracranial and intraperitoneal injections were performed on reporter line mice. **(f)** No crosstalk between GFP and mcherry signal (upper panel) or eGFP and Tomato lectin-Dylight 594 signal (lower panel) **(g)** Raw data of H2GFP signal (i), manually labelled ground truth (ii), StarDist segmentation (iii), and overlay of ground truth (red) and StarDist segmentation (green) (iv). **(h)** Upper panel: Count of manually segmented ground truth nuclei for StarDist training, each color depicts an individual mouse. Lower panel: StarDist nucleus detection accuracy and precision, each bar represents an individual imaging volume.

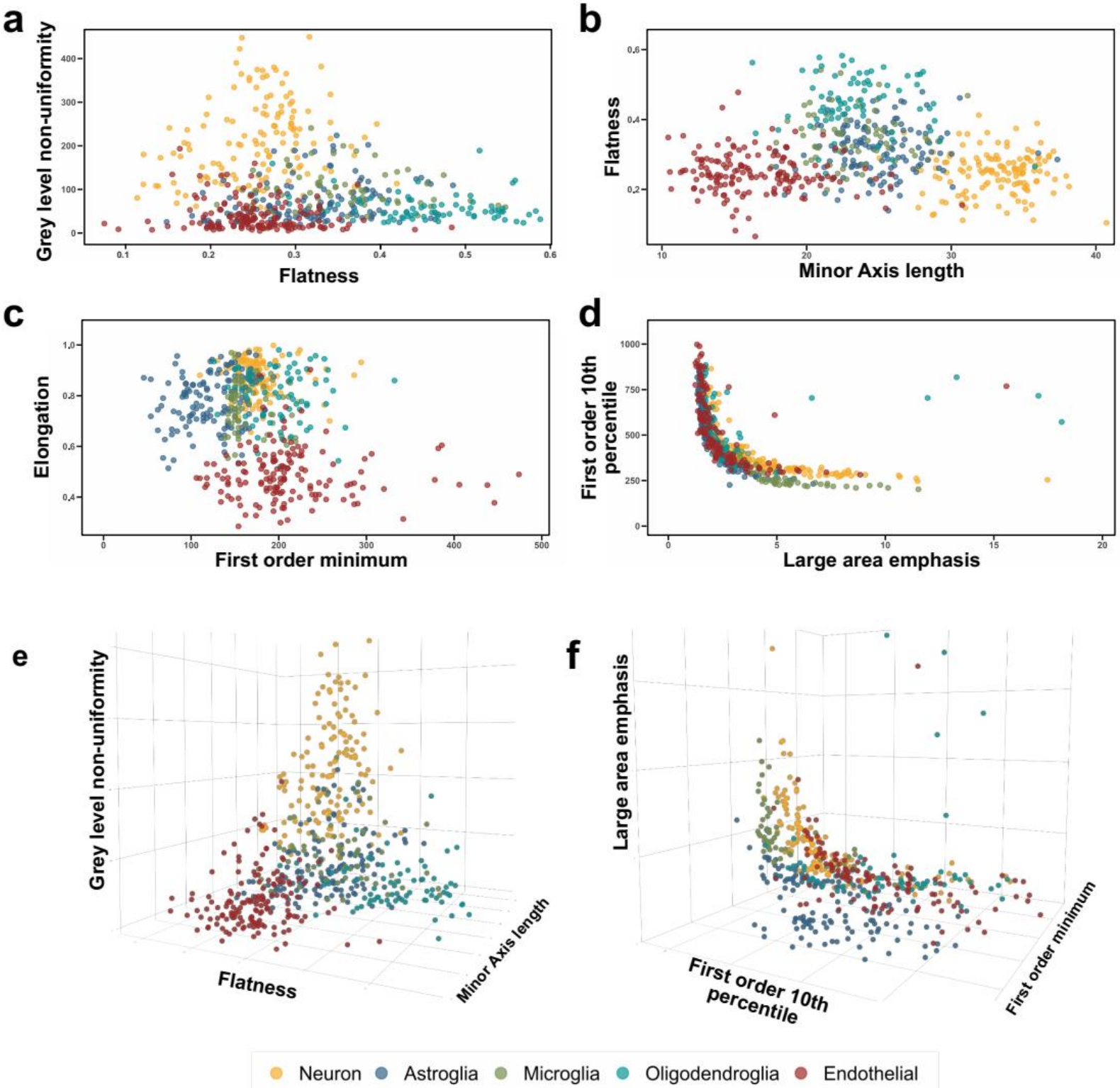
a
Grey level non-uniformity
Flatness
b
Flatness
Minor Axis length
c
Elongation
First order minimum
d
First order 10th percentile
Large area emphasis
e
Grey level non-uniformity
Flatness
Minor Axis length
f
Large area emphasis
First order 10th percentile
First order minimum
Neuron
Astroglia
Microglia
Oligodendroglia
Endothelial

540

541 **Supplementary Figure 2.** Combinations of nuclear morphology, intensity, and texture features
542 show clear distinction between cell types. **(a)** Flatness, gray level non-uniformity. **(b)** Minor axis
543 length, Flatness. **(c)** First order minimum, Elongation. **(d)** Large area emphasis, First order 10th
544 percentile. **(e,f)** Combinations of features in three dimensions. Yellow = Neurons, Blue = Astroglia,
545 Green = Microglia, Turqouise = Oligodendroglia, Red = Endothelial cells. N = Neuron, AGlia =
546 Astroglia, MGlia = Microglia, OGlia = Oligodendroglia, EC = endothelial cells.
547

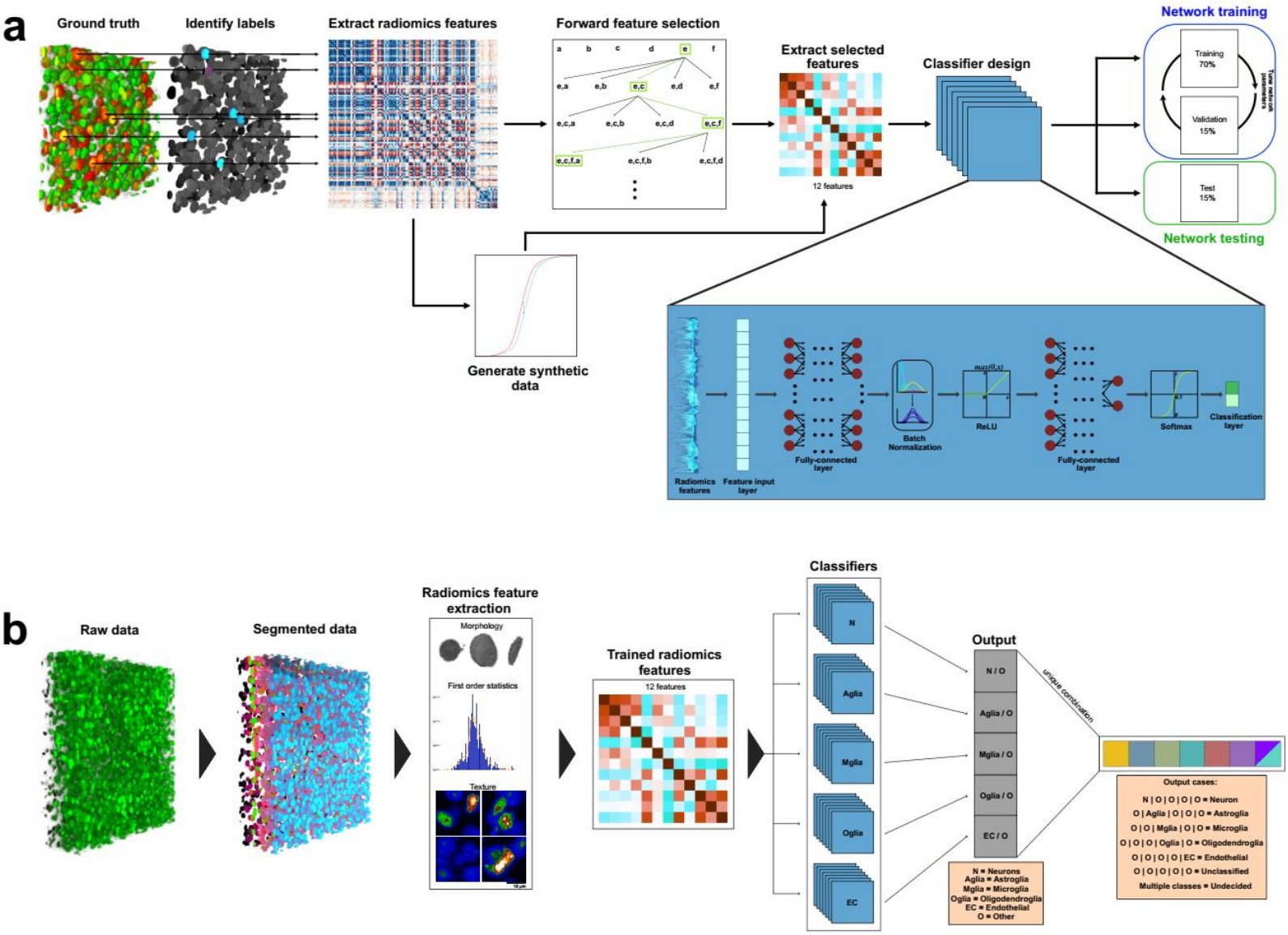

Supplementary Figure 3 (a) For each cell type, green and red channel data from the two-photon volumetric images were overlayed and nuclei labelled in both channels were identified. A sequential forward feature selection algorithm was applied, which selected 12 features from the 107 radiomics feature. Synthetic data was generated from the radiomics features of the original dataset. The combined dataset was used to train a classifier with the training, validation and test data comprising of 70%, 15%, and 15% of the combined dataset, respectively. **(b)** For

classification, volumetric data from H2GFP mice were segmented, radiomics features were extracted and only 12 features from the training were selected. The data was analyzed by all 5 classifiers (one for each cell type) and the outputs of the classifier were combined for each nucleus.

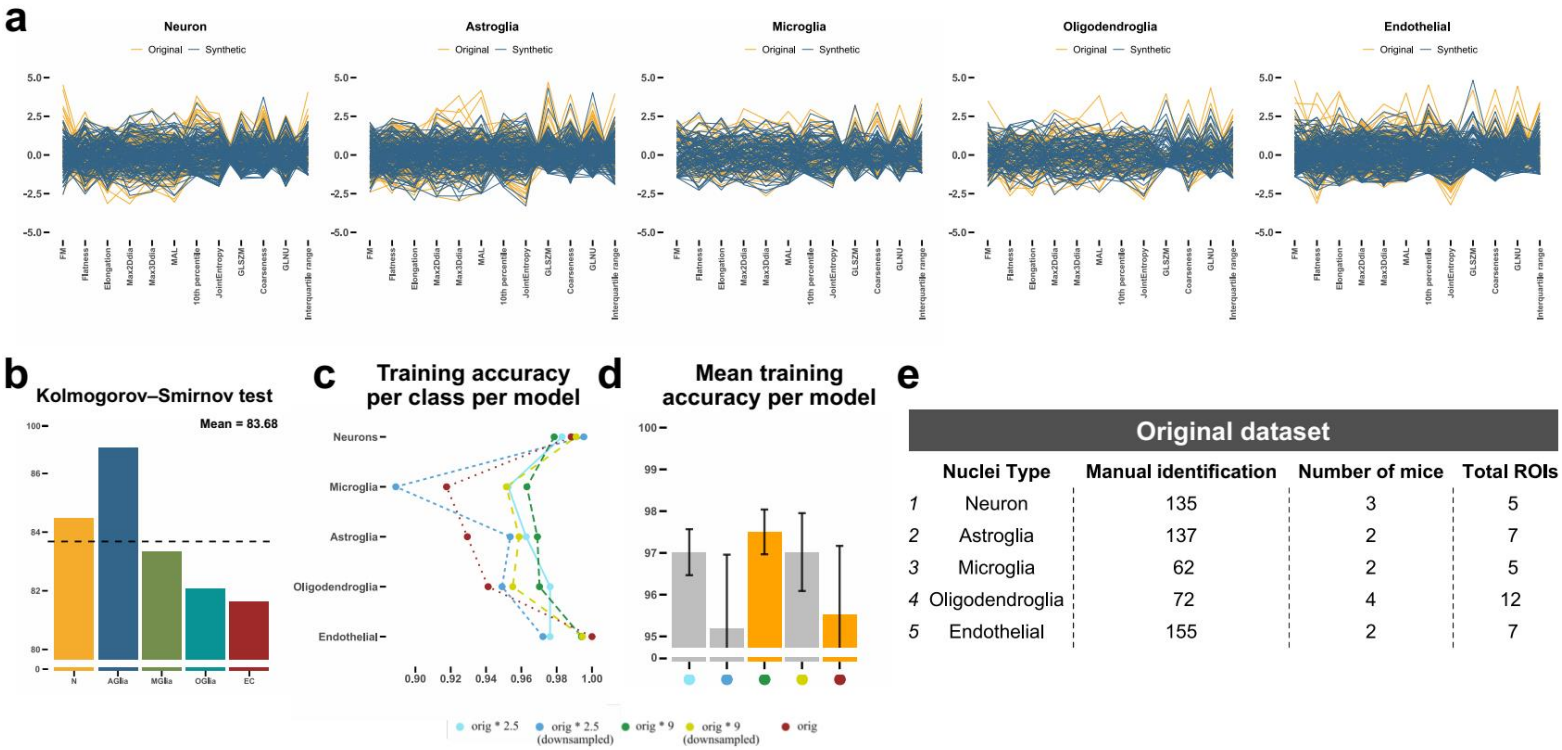

Original dataset				
	Nuclei Type	Manual identification	Number of mice	Total ROIs
1	Neuron	135	3	5
2	Astroglia	137	2	7
3	Microglia	62	2	5
4	Oligodendroglia	72	4	12
5	Endothelial	155	2	7

Supplementary Figure 4. Synthetic training data was generated from the original dataset. **(a)** Distribution of synthetic data is comparable to original data, yellow = original data, blue = synthetic data. **(b)** Statistical analysis of similarity between the distribution of original data and distribution of synthetic data (K-S test; mean = 83.68%). **(c)** Datasets with different amounts of synthetic data were created and the training accuracy was compared between them, orig = original dataset, orig * 2.5 = dataset containing 2.5 times the amount of data as the original dataset, orig * 2.5 (down sampled) = dataset down sampled to original size from the dataset containing 2.5 times the amount of data as the original dataset, orig * 9 = dataset containing 9 times the amount of data as the original dataset, orig * 9 (down sampled) = dataset down sampled to original size from the dataset containing 9 times the amount of data as the original dataset. **(d)** Mean accuracy of classifiers trained on different datasets, light blue = orig * 2.5, dark

blue = orig * 2.5 (downsampled), green = orig * 9, yellow = orig * 9 (down sampled), red = orig.

(e) Table of manually identified nuclei belonging to each cell type.

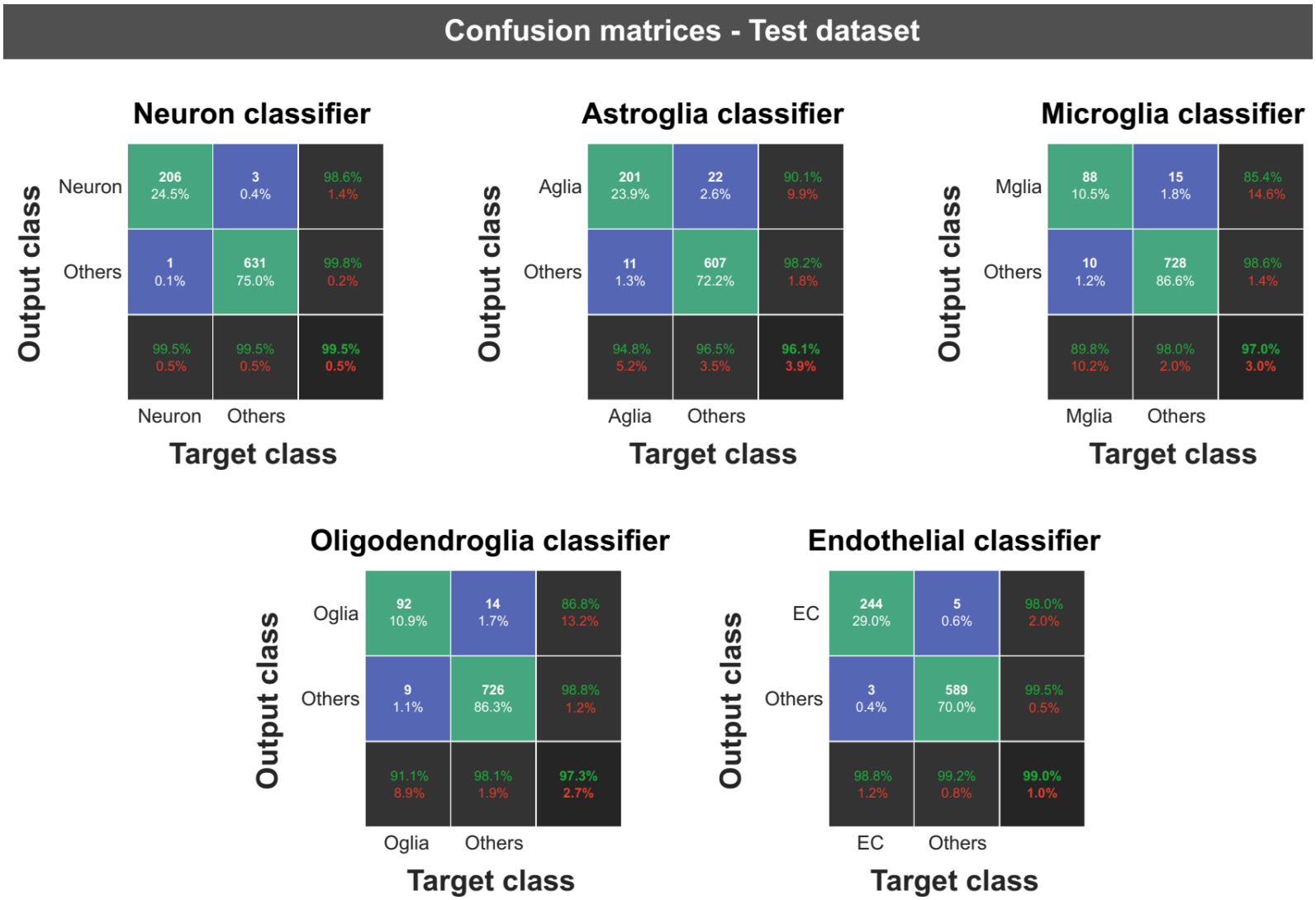

Supplementary Figure 5. Confusion matrices for each classifier for the test dataset. On the y-axis the output class of the classifier is shown, on the x-axis the target class. As the classifier distinguishes between the desired class and the "other" class, the confusion matrix consists only of 4 fields. Green fields illustrate correct identification of target and "other" class, blue fields illustrate erroneous identifications. AGlia = Astroglia, MGlia = Microglia, OGlia = Oligodendroglia, EC = endothelial cells.

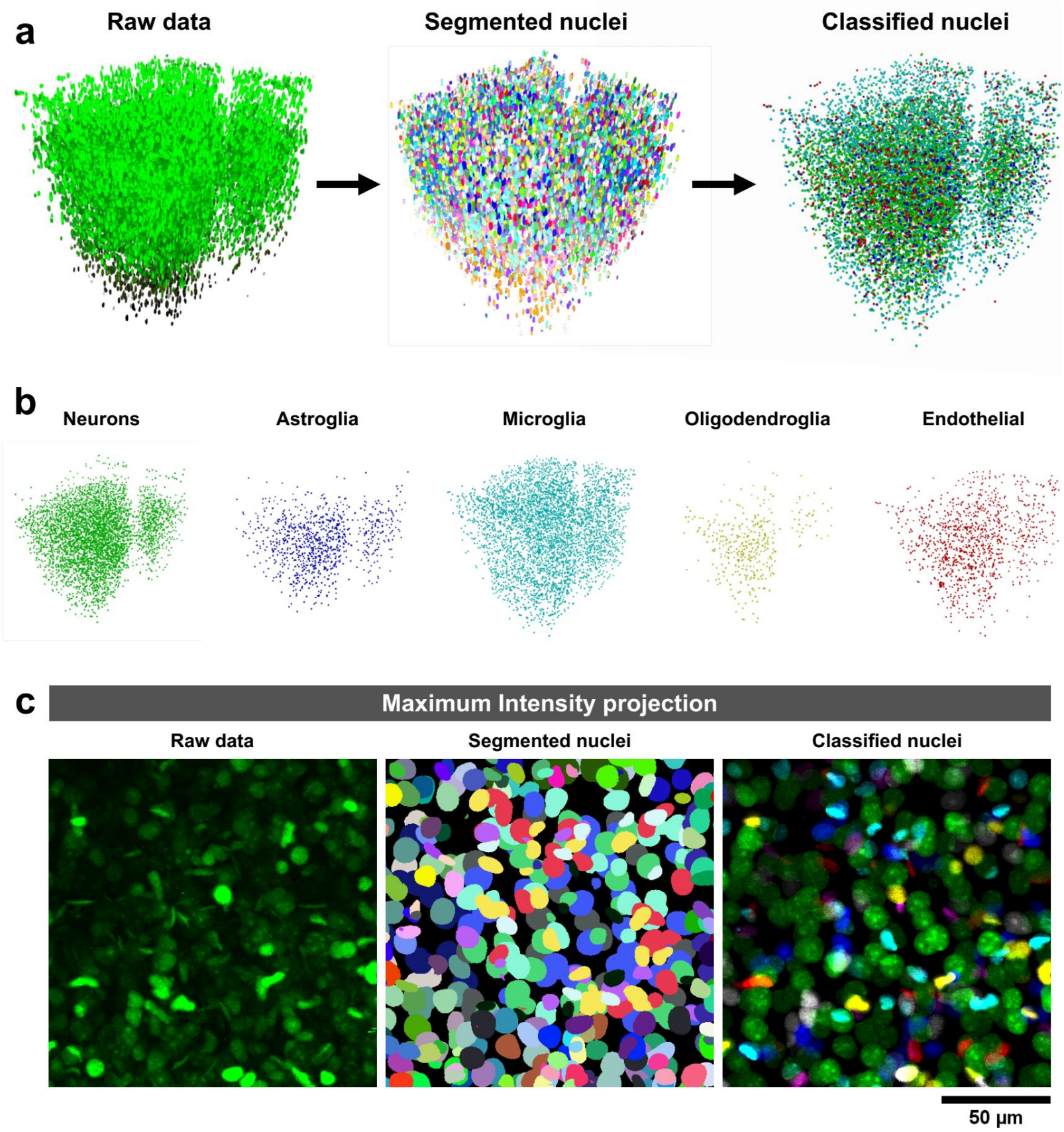
a
Raw data
Segmented nuclei
Classified nuclei
b
Neurons
Astroglia
Microglia
Oligodendroglia
Endothelial
c
Maximum Intensity projection
Raw data
Segmented nuclei
Classified nuclei
50 µm

596

Supplementary Figure 6. 3D visualization of comprehensive cell type composition. (a) 3-dimensional visualization of raw, segmented and classified data (700 µm x 700 µm x 700 µm volume). **(b)** Nuclei distribution for each cell type after classification. **(c)** Maximum intensity z-projection of a sub volume (150 µm x 150 µm x 100 µm) showing raw, segmented and classified nuclei.

Radiomics features							
Morphology		Intensity	Texture				
2-Dimensional	3-Dimensional	First Order Statistics	Gray Level Co-occurence Matrix (GLCM)	Gray Level Run Length Matrix (GLRLM)	Gray Level Size Zone Matrix (GLSZM)	Neighboring Gray Tone Different Matrix (NGTDM)	Gray Level Dependence Matrix (GLDM)
Mesh Surface	Mesh Volume	Energy	Autocorrelation	Short Run Emphasis (SRE)	Small Area Emphasis (SAE)	Coarseness	Small Dependence Emphasis (SDE)
Pixel Surface	Voxel Volume	Total Energy	Joint Average	Long Run Emphasis (LRE)	Large Area Emphasis (LAE)	Contrast	Large Dependence Emphasis (LDE)
Perimeter	Surface Area	Entropy	Cluster Prominence	Gray Level Non-Uniformity (GLN)	Gray Level Non-Uniformity (GLN)	Busyness	Gray Level Non-Uniformity (GLN)
Perimeter to Surface ratio	Surface Area to Volume ratio	Minimum	Cluster Shade	Gray Level Non-Uniformity Normalized (GLNN)	Gray Level Non-Uniformity Normalized (GLNN)	Complexity	Dependence Non-Uniformity (DN)
Sphericity	Sphericity	10th percentile	Cluster Tendency	Run Length Non-Uniformity (RLN)	Size-Zone Non-Uniformity (SZN)	Strength	Dependence Non-Uniformity Normalized (DNN)
Spherical Disproportion	Compactness 1	90th percentile	Contrast	Run Length Non-Uniformity Normalized (RLNN)	Size-Zone Non-Uniformity Normalized (SZNN)		Gray Level Variance (GLV)
Maximum 2D diameter	Compactness 2	Maximum	Correlation	Run Percentage (RP)	Zone Percentage (ZP)		Dependence Variance (DV)
Major Axis Length	Spherical Disproportion	Mean	Difference Average	Gray Level Variance (GLV)	Gray Level Variance (GLV)		Dependence Entropy (DE)
Minor Axis Length	Maximum 3D diameter	Median	Difference Entropy	Run Variance (RV)	Zone Variance (ZV)		Low Gray Level Emphasis (LGLE)
Elongation	Maximum 2D diameter (Slice)	Interquartile Range	Difference Variance	Run Entropy (RE)	Zone Entropy (ZE)		High Gray Level Emphasis (HGLE)
	Maximum 2D diameter (Column)	Range	Joint Energy	Low Gray Level Run Emphasis	Low Gray Level Zone Emphasis		Small Dependence Low Gray Level Emphasis
	Maximum 2D diameter (Row)	Mean Absolute Deviation (MAD)	Joint Entropy	High Gray Level Run Emphasis	High Gray Level Zone Emphasis		Small Dependence High Gray Level Emphasis
	Major Axis Length	Robust Mean Absolute Deviation (rMAD)	Informational Measure of Correlation (IMC) 1	Short Run Low Gray Level Emphasis	Small Area Low Gray Level Emphasis		Large Dependence Low Gray Level Emphasis
	Minor Axis Length	Root Mean Squared (RMS)	Informational Measure of Correlation (IMC) 2	Short Run High Gray Level Emphasis	Small Area High Gray Level Emphasis		Large Dependence High Gray Level Emphasis
	Least Axis Length	Standard Deviation	Inverse Difference Moment (IDM)	Long Run Low Gray Level Emphasis	Large Area Low Gray Level Emphasis		
	Elongation	Skewness	Maximal Correlation Coefficient (MCC)	Long Run High Gray Level Emphasis	Large Area High Gray Level Emphasis		
	Flatness	Kurtosis	Inverse Difference Moment Normalized (IDMN)				
		Variance	Inverse Difference (ID)				
		Uniformity	Inverse Difference Normalized (IDN)				
			Inverse Variance				
			Maximum Probability				
			Sum Average				
			Sum Entropy				
			Sum of Squares				

Supplementary Table 1: Features marked in green were used for cell type classification

Selected Features			Definition
Morphology	3-Dimensional	Maximum 3D diameter	Largest pairwise Eucledian distance between two surface vertices
		Maximum 2D diameter (Row)	Largest pairwise Eucledian distance between two surface vertices in the sagittal plane
		Minor Axis Length	Second largest axis length of the ROI-enclosing ellipsoid
		Elongation	Relationship between two largest principal components in the ROI
		Flatness	Relationship between the largest and the smallest principal components in the ROI
Intensity	First order statistics	Minimum	Minimum gray level intensity within the ROI
		10th percentile	10th percentile of all the voxels in the ROI
		Interquartile Range	Difference between the 75th and 25th Percentile
Texture	Gray Level Co-occurence Matrix (GLCM)	Joint Entropy	Measure of randomness or variability in the neighborhood intensity values
	Gray Level Run Length Matrix (GLRLM)	Gray Level Non-Uniformity (GLN)	Similarity of gray-level intensity values in the image
	Gray Level Size Zone Matrix (GLSZM)	Large Area Emphasis (LAE)	Measures the distribution of large area size zones. Higher value indicates more coarseness
	Neighboring Gray Tone Difference Matrix (NGTDM)	Coarseness	Measures the average difference between the center voxel and its neighborhood

613 **Supplementary Table 2:** Morphology, intensity and texture features used for classification

614

615 **Supplementary Movie 1. Illustration of nucleus segmentation and classification using NuClear.**

616 Raw data of Histon-2B-eGFP-labeled nuclei (green), nucleus segmentation (randomly colored)

617 and classification (apricot = neurons, red = microglia, blue = oligodendrocyts, dark green =

618 astrocytes, magenta = endothelial cells)